

# Detection of ionized hydrogen and oxygen from a very luminous and young galaxy 13.4 billion years ago

Jorge A. Zavala<sup>1</sup>, Marco Castellano<sup>2</sup>, Hollis B. Akins<sup>3</sup>, Tom J. L. C. Bakx<sup>4</sup>, Denis Burgarella<sup>5</sup>, Caitlin M. Casey<sup>3</sup>, Óscar A. Chávez Ortiz<sup>3</sup>, Mark Dickinson<sup>6</sup>, Steven L. Finkelstein<sup>3</sup>, Ikki Mitsuhashi<sup>1,7</sup>, Kimihiko Nakajima<sup>1</sup>, Pablo G. Pérez-González<sup>8</sup>, Pablo Arrabal Haro<sup>6</sup>, Veronique Buat<sup>5</sup>, Bren Backhaus<sup>9</sup>, Antonello Calabrò<sup>2</sup>, Nikko J. Cleri<sup>10,11</sup>, David Fernández-Arenas<sup>12,13</sup>, Adriano Fontana<sup>2</sup>, Maximilien Franco<sup>3</sup>, Mauro Giavalisco<sup>14</sup>, Norman A. Grogin<sup>15</sup>, Nimish Hathi<sup>15</sup>, Michaela Hirschmann<sup>16,17</sup>, Ryota Ikeda<sup>1</sup>, Intae Jung<sup>15</sup>, Jeyhan S. Kartaltepe<sup>18</sup>, Anton M. Koekemoer<sup>15</sup>, Rebecca L. Larson<sup>3,18</sup>, Jed McKinney<sup>3</sup>, Casey Papovich<sup>19,20</sup>, Toshiki Saito<sup>1</sup>, Paola Santini<sup>2</sup>, Roberto Terlevich<sup>21,22,23</sup>, Elena Terlevich<sup>21,23</sup>, Tommaso Treu<sup>24</sup>, and L. Y. Aaron Yung<sup>15</sup>

(Affiliations are included at the end of the document)

**The James Webb Space Telescope (JWST) has discovered a surprising population of bright galaxies in the very early universe ( $\lesssim 500$  Myrs after the Big Bang) that is hard to explain with conventional galaxy formation models and whose physical properties remain to be fully understood. Insight into the internal physics of galaxies is captured best via observations of excited-state atomic transitions of ionized gas, but beyond  $z \approx 7 - 9$ , the brightest spectral signatures are redshifted into the mid-infrared regime, where observations are increasingly more difficult. Here, we present the first detection of a hydrogen recombination line ( $H\alpha$ ) and doubly-ionized oxygen ([OIII]4959,5007 Å) at  $z > 10$  using the JWST Mid-Infrared Instrument, MIRI. These detections place the bright galaxy GHZ2/GLASS-z12 at  $z = 12.33 \pm 0.02$ , making it the most distant astronomical object with direct spectroscopic detection of these lines and the brightest confirmed object at this epoch. These observations provide key insights into the conditions of this primeval galaxy, which shows hard ionizing conditions rarely seen in the local Universe and likely driven by compact, young ( $\lesssim 30$  Myr) star formation. Its oxygen-to-hydrogen abundance is close to a tenth of the solar value, indicating a rapid metal enrichment during the earliest phases of galaxy formation. This study confirms the unique conditions of the brightest and most distant galaxies recently discovered by JWST and the huge potential of mid-IR observations to characterize these systems, opening a range of new possibilities in the study of the very early Universe.**

Following the confirmation of the first surprisingly bright galaxies at high-redshifts ( $z \gtrsim 10$ )<sup>1-3</sup>, research efforts must now shift towards gaining a deeper understanding of their

physical properties. The detection and interpretation of emission-line spectra are pivotal in this topic, with well-studied calibrations and diagnostic diagrams based on rest-frame optical transitions and line ratios such as [NII]/ $H\alpha$  vs [OIII]/ $H\beta$  (typically known as the Baldwin, Phillips and Terlevich<sup>4</sup>, BPT, diagrams). The advent of the JWST and, particularly, the sensitive Near Infrared Spectrograph (NIRSpec), has now unlocked access to some of these lines in very high-redshift galaxies, enabling detailed studies that were previously unreachable beyond  $z \sim 3$  (e.g.<sup>5-10</sup>). At redshifts above  $z \sim 7$ , however, the  $H\alpha$  transition known as the gold standard to measure young star formation activity, is redshifted beyond the NIRSpec coverage. Similarly, the [OIII] and  $H\beta$  lines, sensitive to metallicity and ionizing conditions, can only be observed up to  $z \sim 9.5$  with this instrument.

The MIRI camera on board JWST is thus the only astronomical instrument with the required wavelength coverage to detect these spectral lines at higher redshifts, critical for characterizing the physical properties of the first galaxies in the universe. While early predictions suggested that their successful detection may require long observing times of several tens of hours<sup>11</sup>, the combination of both the better-than-expected performance of JWST<sup>12</sup> and the remarkably high brightness of the JWST-discovered population of distant galaxies, might have improved the prospects for such studies, making the detection of  $z > 10$  rest-frame optical emission lines more feasible than previously anticipated.

Here, we report the results of the first MIRI spectroscopic observations on a  $z > 10$  galaxy candidate and test the efficiency of MIRI as a *redshift machine*.

We target the galaxy GHZ2/GLASS-z12<sup>13,14</sup> ( $\alpha = 3.498985$ ,  $\delta = -30.324767$ ) with MIRI to blindly search for the brightest nebular emission lines: [OIII]4959,5007Å,  $H\alpha$ ,  $H\beta$  (with the doublets [NII]6548,6583Å and [SII]6716,6731Å also covered but expected to be too faint at high redshifts). The target stands out as the most robust among the extremely distant galaxy candidates found in one of the first sets of deep JWST NIRCам images, part of the GLASS-JWST Early Release Science Program<sup>15</sup>, with a UV magnitude of  $M_{UV} = -20.5$  mag<sup>16</sup>, and a photometric redshift of  $z \approx 12.0 - 12.4$ . The MIRI observations were conducted on October 25-29, 2023, using the low resolution spectrometer (LRS) slit mode (resolving power  $R \approx 50 - 200$ ), with a total integration on-source exposure time of 9 h (see details in the Methods). The main advantage

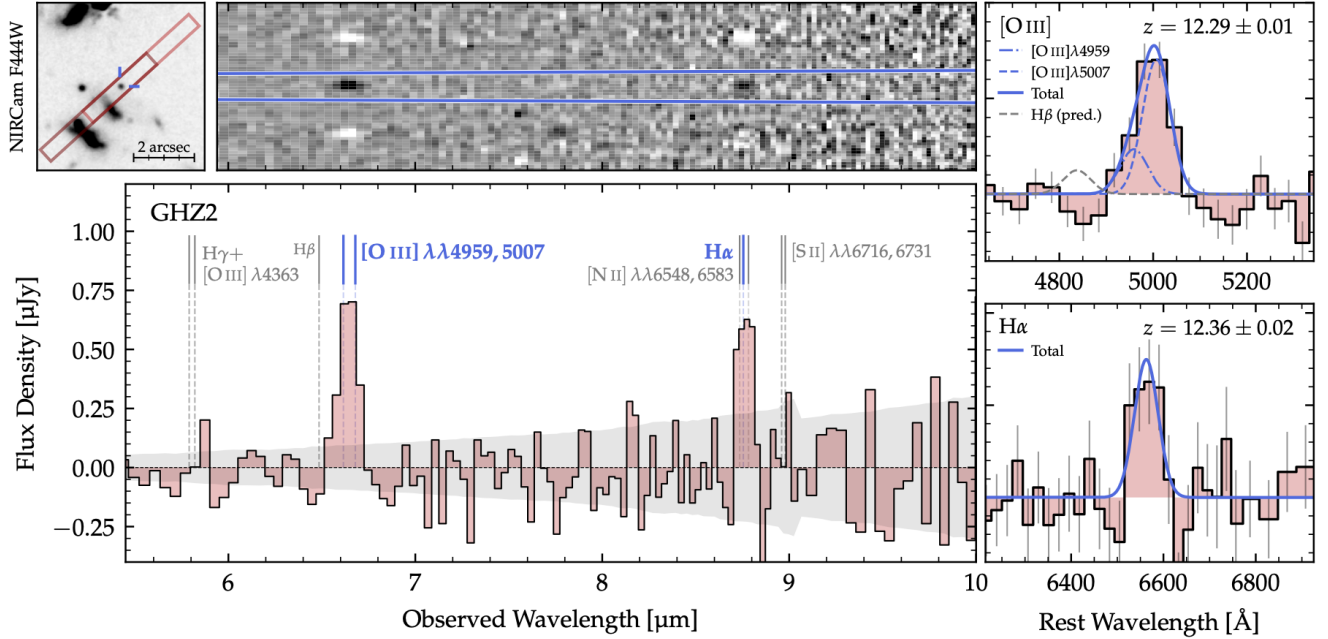


Figure 1: JWST/MIRI spectrum of GHZ2 at  $z = 12.3$ . **Top left:** NIRCам F444W cutout image ( $5'' \times 5''$ ) centered at the position of GHZ2, with the MIRI/LRS slit illustrated with the red rectangle (at the two different dither positions). The combined 2D spectrum and the used aperture for the 1D extraction are also plotted (see details in the Section Methods). **Bottom left:** 1D extracted spectrum at the position of GHZ2 across the most sensitive wavelength range,  $\lambda_{\text{obs}} \approx 5.7 - 10 \mu\text{m}$  and the associated  $1\sigma$  uncertainty (gray region). The redshifted wavelengths of typically bright rest-frame optical emission lines are indicated with the vertical lines, with the blue text highlighting the robust detections. **Right:** Zoom-in on the  $> 5\sigma$  detected spectral features identified as the [OIII]4959,5007Å doublet (*top*) and the H $\alpha$  emission line (*bottom*) along with the best-fit Gaussian functions and the implied redshifts. In the top panel, the predicted H $\beta$  line from the H $\alpha$  detection assuming a dust-free environment is also indicated.

of this mode relies on its large spectral coverage, which provides sensitive observations across  $\approx 5-12 \mu\text{m}$ , covering at least one of the aforementioned lines across  $z \approx 7-20$ . Data reduction was performed using the standard JWST pipeline with some additional steps as described in the Methods.

Figure 1 shows the MIRI one-dimensional (1D) and two-dimensional (2D) spectra of the source. Two spectroscopic features are clearly detected above the noise level ( $> 5\sigma$ ) in the 1D and 2D spectra. These spectral features are associated with the [OIII] doublet (4959Å and 5007Å) and with the H $\alpha$  recombination line, which constrain the redshift of this source to be  $z_{\text{spec}} = 12.33 \pm 0.02$  (see also ref. <sup>16</sup>). This makes this object the most distant galaxy with detections of these emission lines and the brightest among the spectroscopically-confirmed systems at this early epoch. The four other known galaxies with similar spectroscopic redshifts <sup>17-19</sup> ( $z = 12.4 - 13.2$ ) are at least one magnitude fainter and their spectra are distinguished by the lack of strong emission lines. In most of these cases, the spectroscopic redshifts mainly rely on the spectral break produced by the absorption of neutral hydrogen, but extensive tests are needed to rule out lower-redshift solutions that can produce similar breaks. This demonstrates the unique use of MIRI to spectroscopically confirm the most distant galaxies in the

Universe via direct detection of rest-frame optical lines that can additionally provide direct information about the physical properties and chemical abundances of these galaxies.

The emission line around  $6.6 \mu\text{m}$ , associated with the [OIII] doublet, was fitted with a two Gaussian function to infer the line flux densities (reported in Table 1). During this procedure we assume the same line-width for the two lines and fix the relative intensity ratio to the theoretical 1:3 value <sup>20</sup>. In the case of H $\alpha$ , the line was fitted with a single Gaussian function. While we acknowledge that the [NII] doublet are blended with H $\alpha$  emission, at the redshift of GHZ2, where the metallicity is expected to be sub-solar, the contribution from these lines is expected to be negligible <sup>21-23</sup>. This has been proven true even at lower redshifts by JWST/NIRSpec studies of  $z \approx 4 - 7$  galaxies <sup>8,9,24-26</sup> and AGN <sup>27,28</sup>, and even for nitrogen-enriched systems as shown by ref. <sup>26</sup> who measured a line ratio of  $[\text{NII}]/\text{H}\alpha = 2.4 \times 10^{-2}$  in a galaxy at  $z = 6.1$ . Hence, we can safely assume that this line is dominated by the H $\alpha$  emission. For the undetected emission lines, including H $\beta$  and the [SII] doublet,  $2.5\sigma$  upper limits were derived. The detection of H $\alpha$ , however, sets a stronger upper limit on the H $\beta$  flux density assuming a flux ratio of  $\text{H}\alpha/\text{H}\beta = 2.85$  (based on the so-called case-B recombination scenario and

under the typical physical conditions of galaxies’ ionized gas<sup>29</sup>). This ratio is valid in the case of zero dust attenuation, but it increases in the presence of dust since the  $H\beta$  line is more affected by dust extinction. Nevertheless, the dust attenuation is not expected to be significant in this galaxy (see details in the Methods).

This record-breaking detection of  $H\alpha$  provides a direct probe of the young star formation activity, tracing massive stars with ages around or below 10 Myr. This, combined with the detection of oxygen (revealing the presence of metals and thus of more evolved stars), provides a unique opportunity to study the stellar population of this distant galaxy. We infer the average stellar age, and other properties like stellar mass and star formation rate, by conducting spectral energy distribution (SED) fitting to the NIRC*am* photometry jointly with the constraints from the  $H\alpha$  and [OIII] emission lines (see details in the Methods). The photometry and the spectroscopic data are well reproduced with a model with a composite star formation history extending for  $\sim 50$  Myr, with a mass-weighted age of  $28_{-14}^{+10}$  Myr, and more than 60% of the total stellar mass formed during the past 30 Myr. The presence of young and massive stars implies a higher rate of ionizing photon production compared to typical values in galaxies at lower redshifts. The evidence that most of the stellar mass of GHZ2 formed recently is consistent with other results implying that early galaxies have more “bursty” star-formation histories<sup>34–37</sup>). If the majority of early galaxies do indeed form the bulk of their visible mass in their recent past, it could explain not only the remarkable luminosity of this distant galaxy, but the overall surprising number of observed bright galaxies in this epoch<sup>38,39</sup>.

The SED-based SFR (averaged on the last 10 Myr and taking into account the gravitational lensing amplification of  $\mu = 1.3$ <sup>40</sup>) of  $5 \pm 2 M_{\odot} \text{ yr}^{-1}$  is in good agreement with the SFR of  $9 \pm 3 M_{\odot} \text{ yr}^{-1}$  estimated directly from the  $H\alpha$  luminosity assuming the calibration from ref.<sup>41</sup>. This calibration is based on low-metallicity stellar population synthesis models that include the effects of massive stars in binary systems characterized by a high ionizing photon production efficiency. On the other hand, the widely-adopted calibration used for local and low-redshift galaxies<sup>42</sup> predicts a higher SFR of  $\sim 22 \pm 5 M_{\odot} \text{ yr}^{-1}$ , mainly due to the absence of these low-metallicity and binary stars.

The JWST/MIRI data also constrain the  $R3 \equiv \log([\text{OIII}]/H\beta)$  ratio, which is known to correlate with the gas-phase metallicity<sup>43,44</sup>. The estimated line ratio and its associated uncertainty of  $[\text{OIII}]/H\beta = 5.2 \pm 1.5$  (when assuming directly the inferred  $H\beta$  in the case of zero dust attenuation) implies a metallicity of  $12 + \log(\text{O}/\text{H}) = 7.40_{-0.37}^{+0.52}$  according to the relation presented by ref.<sup>45</sup>, corresponding to  $Z = 0.05_{-0.03}^{+0.12} Z_{\odot}$ . A similar range of metallicities are obtained when using the theoretical calibrations<sup>46</sup>

specifically designed for galaxies at  $z > 4$  (see details in the Methods). These values are in good agreement with the independent metallicity estimation of  $12 + \log(\text{O}/\text{H}) = 7.26_{-0.24}^{+0.27}$  based on the  $[\text{NeIII}]3868\text{\AA}/[\text{OII}]3727\text{\AA}$  index (with additional constraints from other lines), as reported in our parallel analysis of the NIRS*pec* data of this source<sup>16</sup>.

Despite the young age derived for GHZ2, it is notable that its metallicity is already enriched to a few percent (or even up to  $\sim 10 - 15\%$ ) of the solar value, significantly above expectations for the primordial objects dominated by the first-generation stars (typically known as population-III stars). This implies a very rapid metal enrichment during the earliest phases of galaxy formation. The metallicity inferred for GHZ2 is higher than the metallicities of the  $z = 10 - 13$  galaxies discovered in the JADES survey<sup>17</sup>. This is not totally surprising since a correlation between stellar mass and metallicity is known to exist even up to  $z \sim 9$ <sup>30</sup>, and the stellar mass of GHZ2 of  $\log(M_{\star}/M_{\odot}) \approx 8.6 - 9.0$  is around an order of magnitude larger than what was inferred for JADES galaxies. Therefore, these results suggest that the mass-metallicity relation exists even up to  $z \sim 12 - 13$ , but shifted towards lower metallicity values (by  $\sim 0.5$  dex) compared to the relationships at  $z < 9$ , as shown in Figure 2.

To gain further insights into the physical conditions of the ionized gas in this galaxy, we show in Figure 2 the well-studied  $[\text{NII}]/H\alpha$  vs  $[\text{OIII}]/H\beta$  BPT-diagram along with the predictions from a photoionization model powered by star formation<sup>47</sup>. The  $R3$  value of  $5.2 \pm 1.5$  derived above implies a high ionization parameter of  $\log(U) \gtrsim -2.0$ , as shown in Figure 2. At the lowest metallicities, the model predictions fail to reproduce the inferred  $R3$  ratio, despite the extreme parameters explored (see details in the Methods section). Higher [OIII]-to- $H\beta$  ratios can be explained by harder ionizing radiation, which might point towards the presence of an active galactic nucleus<sup>22</sup> (i.e. an accreting black hole). Alternatively, harder ionization spectra might be contributed by X-ray binaries or supermassive stars<sup>48–51</sup>. We note that this conclusion is not affected by our assumption of a dust-free environment when calculating the  $H\beta$  line since any dust attenuation will only increase the inferred [OIII]/ $H\beta$  ratio.

This suggestion, combined with the fact that AGN systems occupy a similar parameter space than star-forming galaxies<sup>27,28,52,53</sup> at high redshifts, opens the question whether GHZ2 might be rather powered by AGN activity. Indeed, its NIRS*pec* spectrum<sup>16</sup> shows high ionization lines such as  $\text{NIV}]1488\text{\AA}$  and  $\text{HeII } 1640\text{\AA}$ , requiring ionizing photons with energy above  $\sim 54$  eV, but higher ionizing AGN tracers such as  $[\text{NeIV}]2424\text{\AA}$  and  $[\text{NeV}]3426\text{\AA}$  remain undetected. This prevents us from pinning down the nature of the ionizing source in this system, which could be due to extreme (compact and young) star formation activity, AGN, or a composite system. Similar conclusions

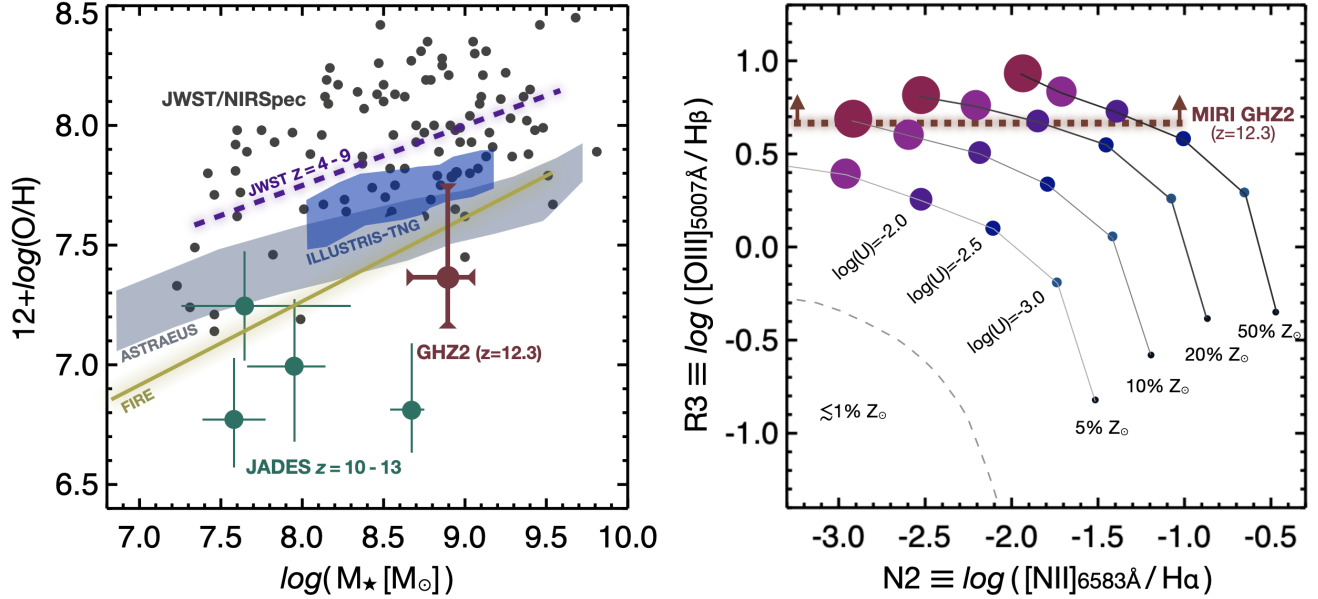


Figure 2: **The stellar mass-metallicity relation and the ionization diagnostic diagram.** **Left:** Position of GHZ2 in the stellar mass-metallicity plane in comparison to lower redshift galaxies at  $z \approx 4 - 9$  (black dots for individual galaxies and purple line for best-fit relationship<sup>30</sup>) and with the  $z = 10 - 13$  galaxies from the JADES survey<sup>17</sup> (green points; metallicity estimated from SED fitting). All the  $z > 10$  galaxies, including GHZ2, are off from the lower-redshift relationship<sup>30</sup>, suggesting an evolution towards lower metallicity values at earlier epochs (by around  $\sim 0.5$  dex). The predictions from the FIRE<sup>31</sup> (golden line) and ASTRAEUS<sup>32</sup> (gray region) simulations at  $z \sim 10$  show a broad agreement with the current constraints, while the ILLUSTRIS-TNG<sup>33</sup> simulations (blue region) predict slightly higher metallicities, although still consistent within the error bars. Despite the early epochs, none of these galaxies show pristine (close-to-zero) metallicities, implying a rapid metal enrichment in the early Universe. **Right:** The  $[\text{NII}]/\text{H}\alpha$  vs  $[\text{OIII}]/\text{H}\beta$  diagram along with the predictions from a stellar photoionization model<sup>22</sup> assuming four different metallicities and six ionization parameters in steps of 0.5dex (models with  $Z \lesssim 0.01 Z_\odot$  would lie below the dashed line). The observational constraints on the R3 value (formally an upper limit) implies high ionizing conditions, with  $\log(U) > -2.0$ .

were reached from a morphological analysis that constrains the size of GHZ2 to be very compact ( $r_e \lesssim 50$  pc) but marginally resolved<sup>54</sup>), consistent with either compact star-formation or a composite AGN/star-forming galaxy system. Further observations are required to pinpoint the nature of this galaxy, but any of the scenarios described above would have strong implications in our understanding of the formation of the most massive galaxies and/or the first black holes of the universe.

It is now useful to put into context the upper limit on the  $[\text{OIII}]\lambda 88\mu\text{m}$  line luminosity derived from previous ALMA observations<sup>55,56</sup>. The line ratio between this and the  $[\text{OIII}]\lambda 5007\text{\AA}$  transition is sensitive to the electron density of the ionized gas with an extra milder dependency on temperature. Figure 3 shows the expected  $[\text{OIII}]\lambda 5007\text{\AA}$ -to- $[\text{OIII}]\lambda 88\mu\text{m}$  line ratio as a function of electron temperature and density (see Methods section for further details). As can be seen, the constraints imposed by the ALMA and JWST observations imply an electron density above  $250 \text{ cm}^{-3}$  (or even above  $10^3 - 10^4 \text{ cm}^{-3}$  for electron temperatures around 6,000-15,000 K). This, again, contrasts with the typical conditions seen in the local Universe and lower redshift galax-

ies with average densities on the order of<sup>57</sup>  $n_e \approx 10^1 - 10^2 \text{ cm}^{-3}$ , but is in agreement with the recent results proving a redshift evolution towards higher electron densities at high redshifts<sup>58</sup>. This evolution might be driven by the higher star formation rate surface density ( $\Sigma_{\text{SFR}}$ ) measured in high-redshift galaxies<sup>25,26,59</sup>, which reach an extreme value above  $\sim 100 M_\odot \text{ yr}^{-1} \text{ kpc}^{-2}$  in GHZ2 (adopting the size from ref.<sup>54</sup>). The combination of these unique conditions, including high ionization parameters, high electron densities, and high star formation rate surface density might explain the brightness of the unique population of  $z > 10$  galaxies recently discovered by JWST, along with the young stellar ages and relatively low metallicities.

This study demonstrates the enormous potential of the Mid-Infrared Instrument, MIRI, on board JWST for the confirmation and characterization of the most distant galaxies in the Universe, allowing studies at redshifts beyond 10 that were previously limited to redshifts less than 7. These observations allow us to determine a robust spectroscopic redshift of  $z = 12.33 \pm 0.02$  for GHZ2, placing this galaxy just  $\sim 400$  Myr after the Big Bang.



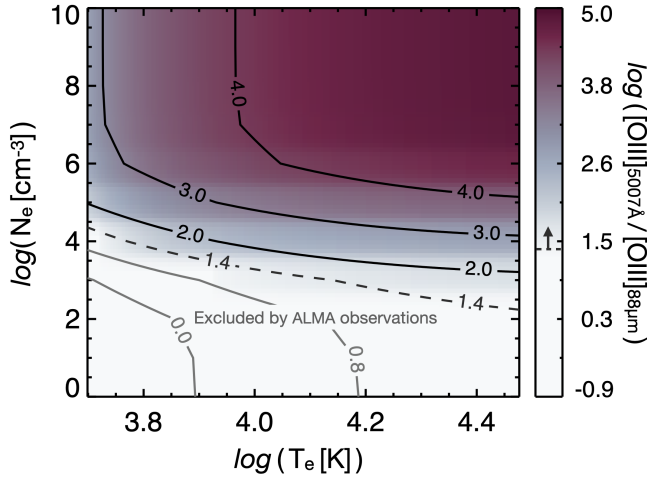


Figure 3: **Electron density constraints.** Predicted [OIII]5007Å-to-[OIII]88 $\mu$ m line ratio (illustrated in different colors and enclosed by the contours) as a function of electron density ( $n_e$ ; y-axis) and electron temperature ( $T_e$ ; x-axis). The combined constraints from the available ALMA observations in combination with the JWST/MIRI data, with  $\log([\text{OIII}]_{5007\text{\AA}}/[\text{OIII}]_{88\mu\text{m}}) > 1.4$ , imply a high electron density of  $> 250 \text{ cm}^{-3}$  (or above  $1,000 \text{ cm}^{-3}$  at  $T_e = 10,000 \text{ K}$ ; see dashed line) that contrasts with local and lower-redshift galaxies, corroborating the extreme conditions of this early galaxy.

GHZ2 is the most distant galaxy with direct detection of several transitions from the ionized gas (see also ref.<sup>16</sup>) and the brightest spectroscopically-confirmed galaxy at this early epoch. The physical conditions of GHZ2, revealed directly by the spectroscopy of the ionized gas, are extreme and rarely seen in the local Universe, with a low (but not pristine) metallicity, high ionization conditions, and high electron density. This emerging picture of compact galaxies with extreme conditions seems to be fairly common at high redshifts, particularly among the brightest systems, and might be associated with short bursts of young star formation with ages of a few tens of Myr and with the presence of massive, low-metallicity stars. Some of the properties of this early galaxy also resemble the observed features of AGN, particularly the hard ionizing spectra inferred from the observations presented here and from the JWST/NIRSpec data<sup>16</sup>. It is thus possible that this source might be, at least partially, powered by an active black hole. Further observations on this and other similar sources will significantly contribute to our understanding of early galaxy formation and black-hole growth, pushing the current frontiers into the formation epoch of the first massive objects in the Universe.

### Acknowledgements

This work is based on observations made with the NASA/ESA/CSA James Webb Space Telescope. The data were obtained from the Mikulski Archive for Space Tele-

scopes at the Space Telescope Science Institute, which is operated by the Association of Universities for Research in Astronomy, Inc., under NASA contract NAS 5-03127 for JWST. These observations are associated with program JWST-ERS-3703. This paper makes use of the following ALMA data: ADS/JAO.ALMA#2021.A.00020.S. ALMA is a partnership of ESO (representing its member states), NSF (USA), and NINS (Japan), together with NRC (Canada), MOST, ASIAA (Taiwan), and KASI (Republic of Korea), in cooperation with the Republic of Chile. The Joint ALMA Observatory is operated by ESO, AUI/NRAO, and NAOJ. JAZ acknowledge funding from JSPS KAKENHI grant number KG23K13150. The GLASS-JWST team acknowledges support by NASA via grant JWST-ERS-1342. Finally, we would like to thank Sarah Kendrew, Greg Sloan, and Milo Docher for their support during the preparation of the observations and their suggestions for data reduction.

1. Arrabal Haro, P. *et al.* Confirmation and refutation of very luminous galaxies in the early Universe. *Nature* **622**, 707–711 (2023).
2. Bunker, A. J. *et al.* JADES NIRSpec Spectroscopy of GN-z11: Lyman- $\alpha$  emission and possible enhanced nitrogen abundance in a  $z = 10.60$  luminous galaxy. *Astron. Astrophys.* **677**, A88 (2023).
3. Harikane, Y. *et al.* Pure Spectroscopic Constraints on UV Luminosity Functions and Cosmic Star Formation History from 25 Galaxies at  $z_{\text{spec}} = 8.61\text{--}13.20$  Confirmed with JWST/NIRSpec. *Astrophys. J.* **960**, 56 (2024).
4. Baldwin, J. A., Phillips, M. M. & Terlevich, R. Classification parameters for the emission-line spectra of extragalactic objects. *PASP* **93**, 5–19 (1981).
5. Backhaus, B. E. *et al.* CEERS Key Paper. VIII. Emission-line Ratios from NIRSpec and NIRCам Wide-Field Slitless Spectroscopy at  $z \lesssim 2$ . *Astrophys. J.* **962**, 195 (2024).
6. Cleri, N. J. *et al.* Using [Ne V]/[Ne III] to Understand the Nature of Extreme-ionization Galaxies. *Astrophys. J.* **953**, 10 (2023).
7. Trump, J. R. *et al.* The Physical Conditions of Emission-line Galaxies at Cosmic Dawn from JWST/NIRSpec Spectroscopy in the SMACS 0723 Early Release Observations. *Astrophys. J.* **945**, 35 (2023).
8. Sanders, R. L., Shapley, A. E., Topping, M. W., Reddy, N. A. & Brammer, G. B. Excitation and Ionization Properties of Star-forming Galaxies at  $z = 2.0\text{--}9.3$  with JWST/NIRSpec. *Astrophys. J.* **955**, 54 (2023).
9. Shapley, A. E., Reddy, N. A., Sanders, R. L., Topping, M. W. & Brammer, G. B. JWST/NIRSpec Measurements of the Relationships between Nebular Emission-line Ratios and Stellar Mass at  $z \approx 3\text{--}6$ . *Astrophys. J. Lett.* **950**, L1 (2023).

10. Chisholm, J. *et al.* [Ne v] emission from a faint epoch of reionization-era galaxy: evidence for a narrow-line intermediate mass black hole. *arXiv e-prints* arXiv:2402.18643 (2024).
11. Rieke, G. H. *et al.* The Mid-Infrared Instrument for the James Webb Space Telescope, I: Introduction. *PASP* **127**, 584 (2015).
12. Rigby, J. *et al.* The Science Performance of JWST as Characterized in Commissioning. *PASP* **135**, 048001 (2023).
13. Castellano, M. *et al.* Early Results from GLASS-JWST. III. Galaxy Candidates at  $z$  9-15. *Astrophys. J. Lett.* **938**, L15 (2022).
14. Naidu, R. P. *et al.* Two Remarkably Luminous Galaxy Candidates at  $z \approx 10$ -12 Revealed by JWST. *Astrophys. J. Lett.* **940**, L14 (2022).
15. Treu, T. *et al.* The GLASS-JWST Early Release Science Program. I. Survey Design and Release Plans. *Astrophys. J.* **935**, 110 (2022).
16. Castellano, M. *et al.* JWST NIRSpec Spectroscopy of the Remarkable Bright Galaxy GHZ2/GLASS-z12 at Redshift 12.34. *submitted* (2024).
17. Curtis-Lake, E. *et al.* Spectroscopic confirmation of four metal-poor galaxies at  $z = 10.3$ -13.2. *Nature Astronomy* **7**, 622–632 (2023).
18. D'Eugenio, F. *et al.* JADES: Carbon enrichment 350 Myr after the Big Bang in a gas-rich galaxy. *arXiv e-prints* arXiv:2311.09908 (2023).
19. Wang, B. *et al.* UNCOVER: Illuminating the Early Universe-JWST/NIRSpec Confirmation of  $z \lesssim 12$  Galaxies. *Astrophys. J. Lett.* **957**, L34 (2023).
20. Storey, P. J. & Zeppen, C. J. Theoretical values for the [OIII] 5007/4959 line-intensity ratio and homologous cases. *Mon. Not. R. Astron. Soc.* **312**, 813–816 (2000).
21. Groves, B. A., Heckman, T. M. & Kauffmann, G. Emission-line diagnostics of low-metallicity active galactic nuclei. *Mon. Not. R. Astron. Soc.* **371**, 1559–1569 (2006).
22. Nakajima, K. & Maiolino, R. Diagnostics for PopIII galaxies and direct collapse black holes in the early universe. *Mon. Not. R. Astron. Soc.* **513**, 5134–5147 (2022).
23. Simmonds, C. *et al.* The ionizing photon production efficiency at  $z$  6 for Lyman-alpha emitters using JEMS and MUSE. *Mon. Not. R. Astron. Soc.* **523**, 5468–5486 (2023).
24. Cameron, A. J. *et al.* JADES: Probing interstellar medium conditions at  $z \sim 5.5$ -9.5 with ultra-deep JWST/NIRSpec spectroscopy. *Astron. Astrophys.* **677**, A115 (2023).
25. Calabrò, A. *et al.* The evolution of the SFR and  $\Sigma_{SFR}$  of galaxies in cosmic morning ( $4 < z < 10$ ). *arXiv e-prints* arXiv:2402.17829 (2024).
26. Topping, M. W. *et al.* Metal-poor star formation at  $z > 6$  with JWST: new insight into hard radiation fields and nitrogen enrichment on 20 pc scales. *arXiv e-prints* arXiv:2401.08764 (2024).
27. Kocevski, D. D. *et al.* Hidden Little Monsters: Spectroscopic Identification of Low-mass, Broad-line AGNs at  $z \lesssim 5$  with CEERS. *Astrophys. J. Lett.* **954**, L4 (2023).
28. Harikane, Y. *et al.* A JWST/NIRSpec First Census of Broad-line AGNs at  $z = 4$ -7: Detection of 10 Faint AGNs with  $M_{BH} 10^6$ - $10^8 M_{\odot}$  and Their Host Galaxy Properties. *Astrophys. J.* **959**, 39 (2023).
29. Osterbrock, D. E. & Ferland, G. J. *Astrophysics of gaseous nebulae and active galactic nuclei* (2006).
30. Nakajima, K. *et al.* JWST Census for the Mass-Metallicity Star Formation Relations at  $z = 4$ -10 with Self-consistent Flux Calibration and Proper Metallicity Calibrators. *Astrophys. J. Suppl.* **269**, 33 (2023).
31. Ma, X. *et al.* The origin and evolution of the galaxy mass-metallicity relation. *Mon. Not. R. Astron. Soc.* **456**, 2140–2156 (2016).
32. Ucci, G. *et al.* Astraevs V: the emergence and evolution of metallicity scaling relations during the epoch of reionization. *Mon. Not. R. Astron. Soc.* **518**, 3557–3575 (2023).
33. Torrey, P. *et al.* The evolution of the mass-metallicity relation and its scatter in IllustrisTNG. *Mon. Not. R. Astron. Soc.* **484**, 5587–5607 (2019).
34. Endsley, R. *et al.* The Star-forming and Ionizing Properties of Dwarf  $z$ -6-9 Galaxies in JADES: Insights on Bursty Star Formation and Ionized Bubble Growth. *arXiv e-prints* arXiv:2306.05295 (2023).
35. Ciesla, L. *et al.* Identification of a transition from stochastic to secular star formation around  $z = 9$  with JWST. *arXiv e-prints* arXiv:2309.15720 (2023).
36. Tacchella, S. *et al.* On the Stellar Populations of Galaxies at  $z = 9$ -11: The Growth of Metals and Stellar Mass at Early Times. *Astrophys. J.* **927**, 170 (2022).
37. Cole, J. W. *et al.* CEERS: Increasing Scatter along the Star-Forming Main Sequence Indicates Early Galaxies Form in Bursts. *arXiv e-prints* arXiv:2312.10152 (2023).
38. Finkelstein, S. L. *et al.* The Complete CEERS Early Universe Galaxy Sample: A Surprisingly Slow Evolution of the Space Density of Bright Galaxies at  $z \sim 8.5$ -14.5. *arXiv e-prints* arXiv:2311.04279 (2023).
39. Adams, N. J. *et al.* EPOCHS Paper II: The Ultraviolet Luminosity Function from  $7.5 < z < 13.5$  using 180 square arcminutes of deep, blank-fields from the PEARLS Survey and Public JWST data. *arXiv e-prints* arXiv:2304.13721 (2023).
40. Bergamini, P. *et al.* The GLASS-JWST Early Release Science Program. III. Strong-lensing Model of Abell 2744 and Its Infalling Regions. *Astrophys. J.* **952**, 84 (2023).
41. Reddy, N. A. *et al.* The Effects of Stellar Population and Gas Covering Fraction on the Emergent Ly $\alpha$  Emission of High-redshift Galaxies. *Astrophys. J.* **926**, 31 (2022).

42. Kennicutt, R. C. & Evans, N. J. Star Formation in the Milky Way and Nearby Galaxies. *Annual Review of Astronomy and Astrophysics* **50**, 531–608 (2012).
43. Nagao, T., Maiolino, R. & Marconi, A. Gas metallicity diagnostics in star-forming galaxies. *Astron. Astrophys.* **459**, 85–101 (2006).
44. Maiolino, R. *et al.* AMAZE. I. The evolution of the mass-metallicity relation at  $z \lesssim 3$ . *Astron. Astrophys.* **488**, 463–479 (2008).
45. Sanders, R. L., Shapley, A. E., Topping, M. W., Reddy, N. A. & Brammer, G. B. Direct  $T_e$ -based Metallicities of  $z = 2$ –9 Galaxies with JWST/NIRSpec: Empirical Metallicity Calibrations Applicable from Reionization to Cosmic Noon. *Astrophys. J.* **962**, 24 (2024).
46. Hirschmann, M., Charlot, S. & Somerville, R. S. High-redshift metallicity calibrations for JWST spectra: insights from line emission in cosmological simulations. *Mon. Not. R. Astron. Soc.* **526**, 3504–3518 (2023).
47. Nakajima, K. *et al.* EMPRESS. V. Metallicity Diagnostics of Galaxies over  $12 + \log(\text{O}/\text{H}) = 6.9$ –8.9 Established by a Local Galaxy Census: Preparing for JWST Spectroscopy. *Astrophys. J. Suppl.* **262**, 3 (2022).
48. Schaerer, D., Fragos, T. & Izotov, Y. I. X-ray binaries as the origin of nebular He II emission in low-metallicity star-forming galaxies. *Astron. Astrophys.* **622**, L10 (2019).
49. Simmonds, C., Schaerer, D. & Verhamme, A. Can nebular He II emission be explained by ultra-luminous X-ray sources? *Astron. Astrophys.* **656**, A127 (2021).
50. Lecroq, M. *et al.* Nebular emission from young stellar populations including binary stars. *Mon. Not. R. Astron. Soc.* **527**, 9480–9504 (2024).
51. Upadhyaya, A. *et al.* Evidence for Very Massive Stars in extremely UV-bright star-forming galaxies at  $z \sim 2.2 - 3.6$ . *arXiv e-prints* arXiv:2401.16165 (2024).
52. Hirschmann, M. *et al.* Synthetic nebular emission from massive galaxies - II. Ultraviolet-line diagnostics of dominant ionizing sources. *Mon. Not. R. Astron. Soc.* **487**, 333–353 (2019).
53. Übler, H. *et al.* GA-NIFS: A massive black hole in a low-metallicity AGN at  $z \sim 5.55$  revealed by JWST/NIRSpec IFS. *Astron. Astrophys.* **677**, A145 (2023).
54. Ono, Y. *et al.* Morphologies of Galaxies at  $z \gtrsim 9$  Uncovered by JWST/NIRCam Imaging: Cosmic Size Evolution and an Identification of an Extremely Compact Bright Galaxy at  $z$  12. *Astrophys. J.* **951**, 72 (2023).
55. Bakx, T. J. L. C. *et al.* Deep ALMA redshift search of a  $z$  12 GLASS-JWST galaxy candidate. *Mon. Not. R. Astron. Soc.* **519**, 5076–5085 (2023).
56. Popping, G. An upper limit on [O III] 88  $\mu\text{m}$  and 1.2 mm continuum emission from a JWST  $z \approx 12$ –13 galaxy candidate with ALMA. *Astron. Astrophys.* **669**, L8 (2023).
57. Kaasinen, M., Bian, F., Groves, B., Kewley, L. J. & Gupta, A. The COSMOS-[O II] survey: evolution of electron density with star formation rate. *Mon. Not. R. Astron. Soc.* **465**, 3220–3234 (2017).
58. Isobe, Y. *et al.* Redshift Evolution of Electron Density in the Interstellar Medium at  $z$  0–9 Uncovered with JWST/NIRSpec Spectra and Line-spread Function Determinations. *Astrophys. J.* **956**, 139 (2023).
59. Reddy, N. A., Topping, M. W., Sanders, R. L., Shapley, A. E. & Brammer, G. A JWST/NIRSpec Exploration of the Connection between Ionization Parameter, Electron Density, and Star-formation-rate Surface Density in  $z = 2.7$ –6.3 Galaxies. *Astrophys. J.* **952**, 167 (2023).
60. Asplund, M., Grevesse, N., Sauval, A. J. & Scott, P. The Chemical Composition of the Sun. *Annual Review of Astronomy and Astrophysics* **47**, 481–522 (2009).
61. Kendrew, S. *et al.* The Mid-Infrared Instrument for the James Webb Space Telescope, IV: The Low-Resolution Spectrometer. *PASP* **127**, 623 (2015).
62. Beiler, S. A. *et al.* The First JWST Spectral Energy Distribution of a Y Dwarf. *Astrophys. J. Lett.* **951**, L48 (2023).
63. Pillepich, A. *et al.* Simulating galaxy formation with the IllustrisTNG model. *Mon. Not. R. Astron. Soc.* **473**, 4077–4106 (2018).
64. Matthee, J. *et al.* The production and escape of Lyman-Continuum radiation from star-forming galaxies at  $z \sim 2$  and their redshift evolution. *Mon. Not. R. Astron. Soc.* **465**, 3637–3655 (2017).
65. Matthee, J. *et al.* EIGER. II. First Spectroscopic Characterization of the Young Stars and Ionized Gas Associated with Strong H $\beta$  and [O III] Line Emission in Galaxies at  $z = 5$ –7 with JWST. *Astrophys. J.* **950**, 67 (2023).
66. Robertson, B. E. *et al.* New Constraints on Cosmic Reionization from the 2012 Hubble Ultra Deep Field Campaign. *Astrophys. J.* **768**, 71 (2013).
67. Pérez-González, P. G. *et al.* Stellar populations in local star-forming galaxies - I. Data and modelling procedure. *Mon. Not. R. Astron. Soc.* **338**, 508–524 (2003).
68. Pérez-González, P. G. *et al.* The Stellar Mass Assembly of Galaxies from  $z = 0$  to  $z = 4$ : Analysis of a Sample Selected in the Rest-Frame Near-Infrared with Spitzer. *Astrophys. J.* **675**, 234–261 (2008).
69. Pérez-González, P. G. *et al.* What is the nature of Little Red Dots and what is not, MIRI SMILES edition. *arXiv e-prints* arXiv:2401.08782 (2024).
70. Bruzual, G. & Charlot, S. Stellar population synthesis at the resolution of 2003. *Mon. Not. R. Astron. Soc.* **344**, 1000–1028 (2003).
71. Chabrier, G. Galactic Stellar and Substellar Initial Mass Function. *PASP* **115**, 763–795 (2003).

72. Calzetti, D. *et al.* The Dust Content and Opacity of Actively Star-forming Galaxies. *Astrophys. J.* **533**, 682–695 (2000).
73. Ferland, G. J. *et al.* CLOUDY 90: Numerical Simulation of Plasmas and Their Spectra. *PASP* **110**, 761–778 (1998).
74. Chatzikos, M. *et al.* The 2023 Release of Cloudy. *Rev. Mexic. Astron. Astrof.* **59**, 327–343 (2023).
75. Carnall, A. C., McLure, R. J., Dunlop, J. S. & Davé, R. Inferring the star formation histories of massive quiescent galaxies with BAGPIPES: evidence for multiple quenching mechanisms. *Mon. Not. R. Astron. Soc.* **480**, 4379–4401 (2018).
76. Boquien, M. *et al.* CIGALE: a python Code Investigating GALaxy Emission. *Astron. Astrophys.* **622**, A103 (2019).
77. Ferland, G. J. *et al.* The 2017 Release Cloudy. *Rev. Mexic. Astron. Astrof.* **53**, 385–438 (2017).
78. Luridiana, V., Morisset, C. & Shaw, R. A. PyNeb: a new tool for analyzing emission lines. I. Code description and validation of results. *Astron. Astrophys.* **573**, A42 (2015).
79. Yoon, I. *et al.* ALMA Observation of a  $z \gtrsim 10$  Galaxy Candidate Discovered with JWST. *Astrophys. J.* **950**, 61 (2023).



## Affiliations

<sup>1</sup>National Astronomical Observatory of Japan, 2-21-1, Osawa, Mitaka, Tokyo, Japan

<sup>2</sup>INAF - Osservatorio Astronomico di Roma, Via Frascati 33, 00078, Monte Porzio Catone, Italy

<sup>3</sup>Department of Astronomy, The University of Texas at Austin, 2515 Speedway Boulevard Stop C1400, Austin, TX 78712, USA

<sup>4</sup>Department of Space, Earth, & Environment, Chalmers University of Technology, Chalmersplatsen 4, SE-412 96 Gothenburg, Sweden

<sup>5</sup>Aix Marseille Univ, CNRS, CNES, LAM, Marseille, France

<sup>6</sup>NSF's National Optical-Infrared Astronomy Research Laboratory, 950 N. Cherry Avenue, Tucson, AZ 85719, USA

<sup>7</sup>Department of Astronomy, The University of Tokyo, 7-3-1 Hongo, Bunkyo, Tokyo 113-0033, Japan

<sup>8</sup>Centro de Astrobiología (CAB), CSIC-INTA, Ctra. de Ajalvir km 4, Torrejón de Ardoz, E-28850, Madrid, Spain

<sup>9</sup>Department of Physics, 196A Auditorium Road, Unit 3046, University of Connecticut, Storrs, CT 06269, USA

<sup>10</sup>Department of Physics and Astronomy, Texas A&M University, College Station, TX 77843-4242 USA

<sup>11</sup>George P. and Cynthia Woods Mitchell Institute for Fundamental Physics and Astronomy, Texas A&M University, College Station, TX 77843-4242 USA

<sup>12</sup>Canada-France-Hawaii Telescope, Kamuela, HI 96743, USA

<sup>13</sup>Instituto de Radioastronomía y Astrofísica, UNAM Campus Morelia, Apartado postal 3-72, 58090 Morelia, Michoacán, Mexico

<sup>14</sup>University of Massachusetts Amherst, 710 North Pleasant Street, Amherst, MA, 01003-9305, USA

<sup>15</sup>Space Telescope Science Institute, 3700 San Martin Dr, Baltimore, MD 21218, USA

<sup>16</sup>Institute for Physics, Laboratory for Galaxy Evolution and Spectral Modelling, Ecole Polytechnique Federale de Lausanne, Observatoire de Sauverny, Chemin Pegasi 51, 1290 Versoix, Switzerland

<sup>17</sup>INAF, Osservatorio Astronomico di Trieste, Via Tiepolo 11, I-34131 Trieste, Italy

<sup>18</sup>Laboratory for Multiwavelength Astrophysics, School of Physics and Astronomy, Rochester Institute of Technology, 84 Lomb Memorial Drive, Rochester, NY 14623, USA

<sup>19</sup>Department of Physics and Astronomy, Texas A&M University, College Station, TX, 77843-4242 USA

<sup>20</sup>George P. and Cynthia Woods Mitchell Institute for Fundamental Physics and Astronomy, Texas A&M University, College Station, TX, 77843-4242 USA

<sup>21</sup>Instituto Nacional de Astrofísica, Óptica y Electrónica, Tonantzintla, 72840 Puebla, Mexico

<sup>22</sup>Institute of Astronomy, University of Cambridge, Cambridge CB3 0HA, UK

<sup>23</sup>Facultad de Astronomía y Geofísica, Universidad de La Plata, Paseo del Bosque s/n, B1900FWA La Plata, Argentina

<sup>24</sup>Department of Physics and Astronomy, University of California, Los Angeles, 430 Portola Plaza, Los Angeles, CA 90095, USA

## Methods

### A Cosmology and other definitions

Throughout this paper, we assume a flat  $\Lambda$ CDM cosmology with  $\Omega_m = 0.29$ ,  $\Omega_\Lambda = 0.71$  and  $H_0 = 69.6 \text{ km s}^{-1} \text{ Mpc}^{-1}$ ; and a Solar abundance of  $12 + \log(\text{O}/\text{H}) = 8.69$ <sup>60</sup>.

### B JWST/MIRI observations and data reduction

Observations were conducted as part of project GO-3703 (PI: J. Zavala) using the MIRI low resolution spectrometer (with the P750L filter) in slit mode. The target was observed in three different visits using the FASTR1 readout pattern and 121 groups per integration, 16 integration per exposure, and 1 exposure per specification with 2 dither positions "along slit nod". Each visit has an on-source time of 10828.26 s (summing 9 h in total). Target acquisition (TA) observations on a bright star (RA=00h13m58.3s; Dec=-30°20'14.10") were conducted before every visit to ensure the target is placed with subpixel accuracy ( $< 10 \text{ mas}$ ) at the nominal slit center location.

We reduce the MIRI data using the official *JWST* pipeline (Version 1.13.4), Calibration Reference Data System (CRDS) version 11.16.16 and CRDS context `jwst_1174.pmap` to assign the reference files. We adopt the stage 1 pipeline procedures unchanged, resulting in six count-rate images (2 dithers, 3 exposures each). Then, we run the `spec2pipeline` stage, which performs flux calibration and various instrument corrections, separately on the individual count-rate exposures, yielding six individual `s2d` images. Due to the presence of a bright nearby galaxy within the slit in one of the dither positions (see the top-left panel in Figure 1), some residual emission is seen in half of the data. Therefore, we continue to treat each dither position separately, averaging the three exposures for each first and yielding one `s2d` file for each dither. Next, we perform a background subtraction on each dither, separately, rather than simply subtracting the two. This was done using the `Background2D` task in `photutils`, masking a  $r = 3.5$  pixel circular region around the detected emission lines. We estimate the median background using a box size of  $2 \times 2$  pixels. We then input these background-subtracted `s2d` files into the `spec3pipeline` stage, which performs outlier rejection via sigma clipping and combines the two dither positions into a single 2D spectrum. Finally, we perform 1D extraction manually using a boxcar filter with a width that scales with the MIRI PSF FWHM, as shown in the top panel of Figure 1. Above  $9 \mu\text{m}$ , where the noise r.m.s. per channel notably increases (due to the sensitivity of the detector and the higher spectral resolution), we re-bin the data with a 2-channel bin.

### C Spectroscopic redshift and line measurements

**Emission line fitting and line ratios:** A single Gaussian function was used to fit the  $\text{H}\alpha$  line assuming negligible contribution from the [NII] doublet. In the case of the [OIII] doublet, we perform a simultaneous two-Gaussian fitting. During this procedure we assume the same line-width for the two lines (leaving it as a free parameter) and fix the 5007/4959 peak line ratio to 3. We use a Levenberg-Marquardt algorithm to perform non-linear least-square minimization (using the `LMFIT` function). The measured line-widths are consistent with the instrumental resolution<sup>61</sup> of  $R \equiv \Delta\lambda/\lambda \approx 81$  around the position of the [OIII] doublet (vs  $R \approx 83$  from the measured line-width) and 132 around  $\text{H}\alpha$  (with a slightly wider measured line-width corresponding to  $R \approx 103$ ).

To infer an upper limit on the  $\text{H}\beta$  line flux density, we assume the  $2.5\sigma$  r.m.s value as the upper limit for the line peak and the same line-width as the [OIII]5007Å line, which is determined by the line spread function of the instrument. This is a reasonable assumption since the lines are very close in wavelength space and thus the spectral resolution is expected to be very similar. This results in a  $\text{H}\beta$  line flux upper limit of  $2.0 \times 10^{-18} \text{ erg s}^{-1} \text{ cm}^{-2}$ . Alternatively, the  $\text{H}\beta$  line flux density was inferred from the detected  $\text{H}\alpha$  line. In the case of a dust-free environment and Case B recombination-line radiation (see details in ref.<sup>29</sup>), the expected  $\text{H}\alpha$ -to- $\text{H}\beta$  line ratio is 2.85 for  $n_e = 10^4 \text{ cm}^{-3}$  and  $T_e = 10,000 \text{ K}$  (note that this ratio does not change significantly for other values of density and temperature). Under these assumptions, we estimate an integrated line flux density of  $0.9 \times 10^{-18} \text{ erg s}^{-1} \text{ cm}^{-2}$ . We adopt this value along the paper since we do not expect a significant dust attenuation for this galaxy (based on the SED fitting results discussed above, the dust continuum ALMA constraints<sup>55</sup>, and the blue UV slope<sup>16</sup>), but it should be formally considered as upper limit since the  $\text{H}\beta$  line would be fainter in the case of appreciable dust attenuation.

**Spectroscopic redshift.** The dominant uncertainty on the spectroscopic redshift comes from the current MIRI/LRS wavelength calibration. While the current calibration accuracy is estimated to be around  $\pm 20 \text{ nm}$ <sup>1</sup>, this still can introduce a redshift offset of  $\Delta z \sim 0.04$ . A recent calibration update (referenced as `jwst_1174.pmap` in the *JWST* pipeline), introduced a shift of about 50 nm at 6 microns and decreasing to nearly zero at the red end of the spectral range. A similar correction but a bit less extreme in the blue part was independently found by ref.<sup>62</sup> using observations of a Y Dwarf. Fitting the line with a single Gaussian component, we obtain  $z_{\text{H}\alpha} = 12.36 \pm 0.02$  with the updated 2024 *JWST* calibration. For comparison, adopting the

<sup>1</sup><https://www.stsci.edu/news/jwst/2024/updates-to-miri-low-resolution-spectrometer-reference-files>

calibration from ref.<sup>62</sup>, we obtain  $z_{H\alpha} = 12.37 \pm 0.02$ . In the case of the [OIII] doublet, and using a two-Gaussian simultaneous fitting as described above, we obtain  $z_{[\text{OIII}]}$  = 12.29  $\pm$  0.01 using the most recent pipeline calibration, or  $z_{[\text{OIII}]}$  = 12.33  $\pm$  0.01 using an alternative wavelength calibration<sup>62</sup>. The differences between the inferred redshifts are attributed to the current wavelength calibration uncertainty of  $\sim 20$  nm. Across this paper we adopted the average of the redshifts obtained with the official pipeline calibration, resulting in  $z = 12.33 \pm 0.2$ . Similar redshift constraints were derived from the NIRSpect observations<sup>16</sup> with a weighted redshift average between four different emission lines of  $z = 12.342 \pm 0.009$ . A more precise MIRI/LRS wavelength calibration in the future will allow to derive spectroscopic redshifts with better than 1% precision even with the low resolution spectrometer.

## D Inferred parameters from the emission lines.

**Metallicity:** We adopted the recent calibration from ref.<sup>45</sup> based on a sample of 46 galaxies at  $z \approx 2 - 9$  observed with JWST/NIRSpect and with multiple line detections (including temperature-sensitive lines), from which we derive  $12 + \log(\text{O}/\text{H}) = 7.40^{+0.52}_{-0.37}$  taking into account the uncertainty on the [OIII]-to- $H\beta$  line ratio and the observed scatter in the calibration sample. This corresponds to  $Z = 0.05^{+0.12}_{-0.03} Z_{\odot}$ . Using instead the calibration from ref.<sup>47</sup>, calibrated using local analogs, results in a consistent metallicity of  $\sim 0.1 Z_{\odot}$ . We finally use the theoretical predictions for metallicity calibrations of ref.<sup>46</sup>, based on the IllustrisTNG<sup>63</sup> simulations connected to photo-ionisation models and focused only on galaxies at  $z > 4$ . This theoretical calibration implies a metallicity of  $Z = 0.04 \pm 0.02 Z_{\odot}$ .

Note that our assumption of a negligible dust attenuation when estimating the  $H\beta$  line luminosity does not bias the inferred metallicity. This is due to the turnover of the relation at higher metallicities where lower values of [OIII]-to- $H\beta$  are expected (while dust attenuation would imply higher line ratios). This turnover implies, however, a second solution for GHZ2 of  $Z \approx 0.55 Z_{\odot}$ . This value is inconsistent with the independent constraints obtained from the NIRSpect data<sup>16</sup>, with several diagnostics suggesting values around or below  $0.1 Z_{\odot}$ . We can thus conclude that the gas-phase metallicity in GHZ2 is close to the aforementioned value of  $Z = 0.05^{+0.12}_{-0.03} Z_{\odot}$ ; relatively low compared to lower redshift galaxies, but not pristine despite its young age.

**Balmer decrement:** In the presence of dust, the  $H\alpha$ -to- $H\beta$  line ratio is expected to deviate from the theoretical value since the short-wavelength  $H\beta$  transition is more susceptible to dust attenuation. However, while the upper limit on the  $H\beta$  line luminosity is consistent with a dust-free scenario it does not rule out the possibility of dust attenuation. Deeper

observations will be necessary to put any constraints on the presence (or absence) of dust in this galaxy via the Balmer decrement.

**SFR and ionizing photon production efficiency.** As mentioned in the main text, we estimate a SFR of  $12 \pm 4 M_{\odot} \text{ yr}^{-1}$  (or  $9 \pm 3 M_{\odot} \text{ yr}^{-1}$  after taking into account the gravitational magnification of  $\mu = 1.3$  estimated by ref.<sup>40</sup>) using the calibration<sup>41</sup>  $\text{SFR}/L(\text{H}\alpha) = 10^{-41.67} (M_{\odot} \text{ yr}^{-1}) / (\text{erg s}^{-1})$ . This calibration was derived from  $Z = 0.001$  BPASS population synthesis models with an upper-mass IMF cut of  $100 M_{\odot}$  and including the effects of stellar binaries. Using instead the relation of ref.<sup>42</sup>, calibrated for lower redshift systems with close-to-solar metallicity, results in a higher SFR by a factor of  $\sim 2.5$ . This difference is mainly attributed to the absence of low-metallicity stars and binary star interactions that produce higher ionization photons. In addition, we infer the SFR from the SED modelling as described below.

The  $H\alpha$  line luminosity was also used to estimate the ionizing photon production efficiency,  $\xi_{\text{ion}}$ , following ref.<sup>64</sup>, which is related to the number of produced ionizing photons per UV luminosity (or SFR). To be conservative, during this calculation we assume an escape fraction of  $f_{\text{esc}} = 0$  (any other value above zero will result in a higher  $\xi_{\text{ion}}$ ) and a dust attenuation of  $A(\text{V}) = 0.3$  mag (note that the attenuation of the young stellar population inferred from our fiducial SED modelling is  $A(\text{V}) = 0.1$  mag, with other models suggesting even lower values). Under these assumptions, we estimate an ionizing photon production efficiency of GHZ2 to be  $\xi_{\text{ion}} \gtrsim 2 \times 10^{25} \text{ Hz erg}^{-1}$ , as shown in Figure 4.

## E SED fitting

The broad-band spectral energy distribution, jointly with the spectroscopic measurements of the  $H\alpha$  and [OIII] emission lines, were fitted to stellar population and nebular gas emission models to estimate the stellar mass, SFR, and mass-weighted age of GHZ2. The NIRCcam photometry is slightly different from previous estimations<sup>13</sup> since we include new observations obtained in July 2023 (see ref.<sup>16</sup> and Merlin et al. in prep. for further details). We used the SYNTHESIZER-AGN code<sup>67-69</sup>, with the stellar populations models from ref.<sup>70</sup> and with a Chabrier<sup>71</sup> initial mass function with stellar mass limits between 0.1 and  $100 M_{\odot}$ . We probed all sub-solar metallicity models. The star formation history was set to a double burst, each stellar population described by a delayed-exponential law with possible timescales ranging from 1 to 100 Myr, ages from 0.1 Myr to the age of the Universe at  $z = 12.36$ . Each stellar population is allowed to be affected by independent dust attenuations described by Calzetti law<sup>72</sup>, with  $A_{\text{V}}$  values ranging from 0 to 1 mag. Nebular continuum and line emission was mod-

	$H\beta^\dagger$	[OIII]4959Å	[OIII]5007Å	$H\alpha$	[OIII]88 $\mu\text{m}^\ddagger$
Line flux [erg/s/cm <sup>2</sup> ] $\times 10^{-18}$	< 2.0 OR $0.9 \pm 0.2$	$1.6 \pm 0.2$	$4.7 \pm 0.5$	$2.5 \pm 0.7$	< 0.18

Table 1: Measured line flux densities or upper limits without correcting for the potential effect of gravitational amplification ( $\mu \approx 1.3$  according to ref.<sup>40</sup>).

<sup>†</sup>Two values are given: an upper limit directly constrained from the data, and the inferred value from  $H\alpha$  (valid in the case of zero dust attenuation; see text for details).

<sup>‡</sup> From ref.<sup>55</sup>.

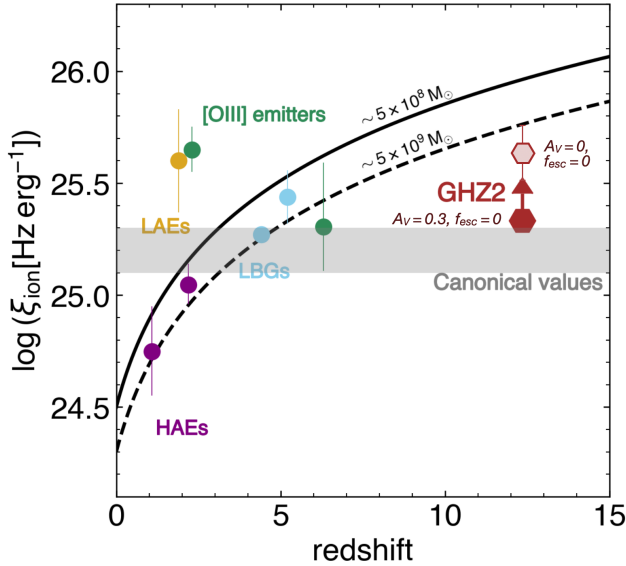


Figure 4: **ionizing photon production efficiency.** Inferred ionizing photon production efficiency for GHZ2 assuming a conservative dust attenuation of  $A(V) = 0.3$  mag (illustrated with the solid hexagon). For comparison, we show the inferred value for a zero dust attenuation (light red) and estimated values for other galaxies (from ref.<sup>65</sup>), along with the redshift evolution from ref.<sup>64</sup>. The bright  $H\alpha$  emission of GHZ2 implies a high ionizing photon production, likely above the typical values adopted for galaxies contributing to the reionization process<sup>66</sup>.

eled with CLOUDY version c23.0.1<sup>73,74</sup>, assuming 10,000 K gas with  $10^4 \text{ cm}^{-3}$  density and abundances linked to the stellar metallicity and ionizing photon flux provided by the stellar models. The main derived properties (without correcting for the gravitational amplification) are: stellar mass  $\log M_*/M_\odot = 9.03^{+0.13}_{-0.28}$ ,  $\text{SFR}_{10\text{Myr}} = 7 \pm 2 M_\odot \text{ yr}^{-1}$ , mass-weighted age  $28^{+10}_{-14}$  Myr. The models also support the low-metallicity directly derived from the [OIII]-to- $H\beta$  line luminosity ratio and the high ionization parameter inferred from the BPT diagram, with a best-fit stellar metallicity of  $Z/Z_\odot = 0.020^{+0.030}_{-0.015}$  and  $\log U = -1.1 \pm 0.4$ . The attenuation for older and younger star populations is constrained to be  $A(V) = 0.3^{+0.1}_{-0.2}$  mag and  $0.1^{+0.2}_{-0.1}$  mag.

Additionally, we use the BAGPIPES<sup>75</sup> and CIGALE<sup>76</sup>

SED-fitting codes with the same stellar population models, IMF, and dust attenuation law. In the case of BAGPIPES we adopt a "bursty continuity" model for the star formation history and found a general good agreement in the age of the stellar population ( $30^{+40}_{-20}$  Myr) with a very similar fraction of mass formed during the last 30 Myr. Other parameters are also consistent within the error bars ( $\log U = -1.4^{+0.2}_{-0.3}$ ;  $\text{SFR} = 2^{+3}_{-1} M_\odot \text{ yr}^{-1}$ ;  $\log M_*/M_\odot = 8.38^{+0.23}_{-0.18}$ ), with the major difference being the close-to-zero attenuation ( $A(V) = 0.01^{+0.02}_{-0.01}$  mag) and a higher metallicity ( $Z = 0.22^{+0.06}_{-0.05}$ ). Similarly, the results with CIGALE implies a mass-weighted stellar age of  $37 \pm 60$  Myr,  $\log M_*/M_\odot = 8.4 \pm 0.5$ ,  $\log U = -2.1^{+0.6}_{-0.3}$ ,  $A(V) = 0.20 \pm 0.28$  mag, and  $\text{SFR}_{10\text{Myr}} = 20 \pm 13 M_\odot \text{ yr}^{-1}$ ; but a significantly higher (and more uncertain) metallicity of  $Z = 0.49^{+0.37}_{-0.20}$ . (Note that all these values are not corrected for gravitational amplification).

While we cannot totally rule out the higher metallicities values inferred from CIGALE and BAGPIPES, we note that these values are at odds with the constraints provided by the [OIII]-to- $H\beta$  ratio and from several other line ratios measured from the NIRSspec spectrum<sup>16</sup>. A more detailed spectro-photometric analysis, combining the NIRCcam photometry with the NIRSspec<sup>16</sup>, MIRI, and ALMA<sup>55</sup> spectroscopy will be necessary to reduce the uncertainties on this and other parameters. This analysis will be presented in a subsequent work (see also Calabro' et al. in prep.).

## F Photoionization and line emissivity models

The photoionization models presented in Figure 2, showing the ratio between [OIII]5007Å and  $H\beta$  and between [NII]6583Å and  $H\alpha$  are taken from ref.<sup>22</sup> and were calculated using the spectral synthesis code, CLOUDY<sup>77</sup>, and assuming the stellar population models from BPASS with a Kroupa IMF with a high-mass cut of  $300 M_\odot$ . In these models, the ionization parameter, defined as the ratio between the hydrogen-ionizing photons and the number density of hydrogen atoms, was varied from -3.5 to -1.0, while the gas electron density was fixed to  $10^3 \text{ cm}^{-3}$ . As seen in Figure 2, the [OIII]5007Å-to- $H\beta$  line ratio of GHZ2 is reproduced only by models with high ionization parameter above -2.0 (in the

case of  $Z \approx 0.1 - 0.2 Z_{\odot}$ ). At the lowest metallicities, the models predictions lie below the inferred value and would require harder ionizing radiation to explain the observational constraints. For instance, AGN-driven models show higher [OIII]5007Å-to-H $\beta$  ratios (by  $\sim 0.3$  dex), when compared with the stellar-driven models at fixed metallicity<sup>22</sup>.

On the other hand, the predicted line ratios between the two transitions of the double-ionized oxygen ([OIII]5007Å and [OIII]88 $\mu$ m) shown in Figure 3 were generated using the PyNeb getEmissivity package<sup>78</sup>, with the default atomic data. The ratio was calculated for different values of electron density and temperature ranging from  $\log(n_e[\text{cm}^{-3}]) = 0 - 10$  and  $\log(T_e[\text{K}]) = 3.6 - 4.6$ . As can be seen in the figure, the ratio is highly sensitive to electron density with a milder dependency on electron temperature (given the significant different energy levels of the two transitions), but independent of metallicity since both transitions arise from the same ion.

## G Revisiting the ALMA data and constraining the electron density

The initial investigation of GHZ2 at sub-mm wavelengths with ALMA only revealed a tentative line<sup>55</sup>, which in hindsight was not at the true redshift of the source. In this work, we use this deep ALMA data to look for the [OIII]88 $\mu$ m emission with the updated redshift information. We investigate the 254.35 GHz region at the position of GHZ2, and find a tentative  $3\sigma$  emission using a single Gaussian fit at the extracted spectrum. If true, this feature provides an order-of-magnitude improvement in the accuracy of the spectroscopic redshift of  $z_{[\text{OIII}]88\mu\text{m}} = 12.339 \pm 0.002$ , in good agreement with the MIRI and NIRSpec-based redshift. Nevertheless, due to the low significance of this detection, here we adopt the previously reported<sup>55</sup> upper limit of  $1.8 \times 10^{-19} \text{ erg s}^{-1} \text{ cm}^{-2}$  (inferred assuming a line-width of 100 km/s). This implies a [OIII]5007Å-to-[OIII]88 $\mu$ m line ratio above 26 ( $\log([\text{OIII}]5007\text{Å}/[\text{OIII}]88\mu\text{m}) > 1.4$ ), which is used in Figure 3 to obtain a strong lower limit on the electron density of  $n_e > 250 \text{ cm}^{-3}$  (or above  $1,000 \text{ cm}^{-3}$  at  $T_e = 10,000 \text{ K}$ ). This is consistent with the picture of higher electron densities at high redshifts, as shown in Figure 6.

High electron densities would naturally explain other non-detections of the [OIII]88 $\mu$ m line at  $z > 10^{79}$  given its relatively low critical density of<sup>29</sup>  $n_c \approx 5 \times 10^2 \text{ cm}^{-3}$ . Above this value, collisional deexcitation plays a significant role in gas cooling, diminishing the line luminosity produced by radiative cooling that is more efficient in the low density regime. Hence, future ALMA follow-up may be more successful by targeting the [OIII]52 $\mu$ m line thanks to its higher critical density of  $n_c \approx 3 \times 10^3 \text{ cm}^{-3}$ .

1. Arrabal Haro, P. *et al.* Confirmation and refutation of very luminous galaxies in the early Universe. *Nature* **622**, 707–711 (2023).
2. Bunker, A. J. *et al.* JADES NIRSpec Spectroscopy of GN-z11: Lyman- $\alpha$  emission and possible enhanced nitrogen abundance in a  $z = 10.60$  luminous galaxy. *Astron. Astrophys.* **677**, A88 (2023).
3. Harikane, Y. *et al.* Pure Spectroscopic Constraints on UV Luminosity Functions and Cosmic Star Formation History from 25 Galaxies at  $z_{\text{spec}} = 8.61\text{--}13.20$  Confirmed with JWST/NIRSpec. *Astrophys. J.* **960**, 56 (2024).
4. Baldwin, J. A., Phillips, M. M. & Terlevich, R. Classification parameters for the emission-line spectra of extragalactic objects. *PASP* **93**, 5–19 (1981).
5. Backhaus, B. E. *et al.* CEERS Key Paper. VIII. Emission-line Ratios from NIRSpec and NIRCам Wide-Field Slitless Spectroscopy at  $z \lesssim 2$ . *Astrophys. J.* **962**, 195 (2024).
6. Cleri, N. J. *et al.* Using [Ne V]/[Ne III] to Understand the Nature of Extreme-ionization Galaxies. *Astrophys. J.* **953**, 10 (2023).
7. Trump, J. R. *et al.* The Physical Conditions of Emission-line Galaxies at Cosmic Dawn from JWST/NIRSpec Spectroscopy in the SMACS 0723 Early Release Observations. *Astrophys. J.* **945**, 35 (2023).
8. Sanders, R. L., Shapley, A. E., Topping, M. W., Reddy, N. A. & Brammer, G. B. Excitation and Ionization Properties of Star-forming Galaxies at  $z = 2.0\text{--}9.3$  with JWST/NIRSpec. *Astrophys. J.* **955**, 54 (2023).
9. Shapley, A. E., Reddy, N. A., Sanders, R. L., Topping, M. W. & Brammer, G. B. JWST/NIRSpec Measurements of the Relationships between Nebular Emission-line Ratios and Stellar Mass at  $z \sim 3\text{--}6$ . *Astrophys. J. Lett.* **950**, L1 (2023).
10. Chisholm, J. *et al.* [Ne v] emission from a faint epoch of reionization-era galaxy: evidence for a narrow-line intermediate mass black hole. *arXiv e-prints* arXiv:2402.18643 (2024).
11. Rieke, G. H. *et al.* The Mid-Infrared Instrument for the James Webb Space Telescope, I: Introduction. *PASP* **127**, 584 (2015).
12. Rigby, J. *et al.* The Science Performance of JWST as Characterized in Commissioning. *PASP* **135**, 048001 (2023).
13. Castellano, M. *et al.* Early Results from GLASS-JWST. III. Galaxy Candidates at  $z \sim 9\text{--}15$ . *Astrophys. J. Lett.* **938**, L15 (2022).
14. Naidu, R. P. *et al.* Two Remarkably Luminous Galaxy Candidates at  $z \approx 10\text{--}12$  Revealed by JWST. *Astrophys. J. Lett.* **940**, L14 (2022).
15. Treu, T. *et al.* The GLASS-JWST Early Release Science Program. I. Survey Design and Release Plans. *Astrophys. J.* **935**, 110 (2022).
16. Castellano, M. *et al.* JWST NIRSpec Spectroscopy of the Remarkable Bright Galaxy GHZ2/GLASS-z12 at Redshift 12.34. *submitted* (2024).



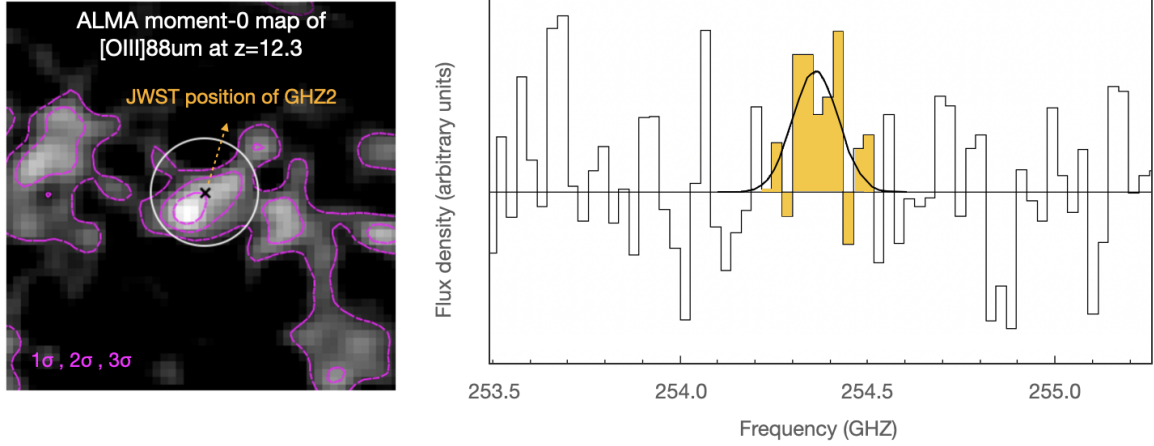


Figure 5: ALMA [OIII]88 $\mu$ m observations at  $z \approx 12.34$ . **Left:** Moment-0 map centered at around 254.5 GHz (the expected frequency of the redshifted [OIII]88 $\mu$ m line), showing a  $\sim 3\sigma$  detection close to the JWST position of our target. **Right:** Extracted spectrum at the position of GHZ2 and best-fit Gaussian function around the expected [OIII]88 $\mu$ m line emission, implying a spectroscopic redshift of  $z_{[\text{OIII}]88\mu\text{m}} = 12.339 \pm 0.002$ .

17. Curtis-Lake, E. *et al.* Spectroscopic confirmation of four metal-poor galaxies at  $z = 10.3$ -13.2. *Nature Astronomy* **7**, 622–632 (2023).
18. D’Eugenio, F. *et al.* JADES: Carbon enrichment 350 Myr after the Big Bang in a gas-rich galaxy. *arXiv e-prints* arXiv:2311.09908 (2023).
19. Wang, B. *et al.* UNCOVER: Illuminating the Early Universe—JWST/NIRSpec Confirmation of  $z \lesssim 12$  Galaxies. *Astrophys. J. Lett.* **957**, L34 (2023).
20. Storey, P. J. & Zeppen, C. J. Theoretical values for the [OIII] 5007/4959 line-intensity ratio and homologous cases. *Mon. Not. R. Astron. Soc.* **312**, 813–816 (2000).
21. Groves, B. A., Heckman, T. M. & Kauffmann, G. Emission-line diagnostics of low-metallicity active galactic nuclei. *Mon. Not. R. Astron. Soc.* **371**, 1559–1569 (2006).
22. Nakajima, K. & Maiolino, R. Diagnostics for PopIII galaxies and direct collapse black holes in the early universe. *Mon. Not. R. Astron. Soc.* **513**, 5134–5147 (2022).
23. Simmonds, C. *et al.* The ionizing photon production efficiency at  $z \sim 6$  for Lyman-alpha emitters using JEMS and MUSE. *Mon. Not. R. Astron. Soc.* **523**, 5468–5486 (2023).
24. Cameron, A. J. *et al.* JADES: Probing interstellar medium conditions at  $z \sim 5.5$ -9.5 with ultra-deep JWST/NIRSpec spectroscopy. *Astron. Astrophys.* **677**, A115 (2023).
25. Calabrò, A. *et al.* The evolution of the SFR and  $\Sigma_{\text{SFR}}$  of galaxies in cosmic morning ( $4 < z < 10$ ). *arXiv e-prints* arXiv:2402.17829 (2024).
26. Topping, M. W. *et al.* Metal-poor star formation at  $z > 6$  with JWST: new insight into hard radiation fields and nitrogen enrichment on 20 pc scales. *arXiv e-prints* arXiv:2401.08764 (2024).
27. Kocevski, D. D. *et al.* Hidden Little Monsters: Spectroscopic Identification of Low-mass, Broad-line AGNs at  $z \lesssim 5$  with CEERS. *Astrophys. J. Lett.* **954**, L4 (2023).
28. Harikane, Y. *et al.* A JWST/NIRSpec First Census of Broad-line AGNs at  $z = 4$ -7: Detection of 10 Faint AGNs with  $M_{\text{BH}} 10^6$ - $10^8 M_{\odot}$  and Their Host Galaxy Properties. *Astrophys. J.* **959**, 39 (2023).
29. Osterbrock, D. E. & Ferland, G. J. *Astrophysics of gaseous nebulae and active galactic nuclei* (2006).
30. Nakajima, K. *et al.* JWST Census for the Mass-Metallicity Star Formation Relations at  $z = 4$ -10 with Self-consistent Flux Calibration and Proper Metallicity Calibrators. *Astrophys. J. Suppl.* **269**, 33 (2023).
31. Ma, X. *et al.* The origin and evolution of the galaxy mass-metallicity relation. *Mon. Not. R. Astron. Soc.* **456**, 2140–2156 (2016).
32. Ucci, G. *et al.* Astraevs V: the emergence and evolution of metallicity scaling relations during the epoch of reionization. *Mon. Not. R. Astron. Soc.* **518**, 3557–3575 (2023).
33. Torrey, P. *et al.* The evolution of the mass-metallicity relation and its scatter in IllustrisTNG. *Mon. Not. R. Astron. Soc.* **484**, 5587–5607 (2019).
34. Endsley, R. *et al.* The Star-forming and Ionizing Properties of Dwarf  $z$ -6-9 Galaxies in JADES: Insights on Bursty Star Formation and Ionized Bubble Growth. *arXiv e-prints* arXiv:2306.05295 (2023).
35. Ciesla, L. *et al.* Identification of a transition from stochastic to secular star formation around  $z = 9$  with JWST. *arXiv e-prints* arXiv:2309.15720 (2023).
36. Tacchella, S. *et al.* On the Stellar Populations of Galaxies at  $z = 9$ -11: The Growth of Metals and Stellar Mass at Early Times. *Astrophys. J.* **927**, 170 (2022).



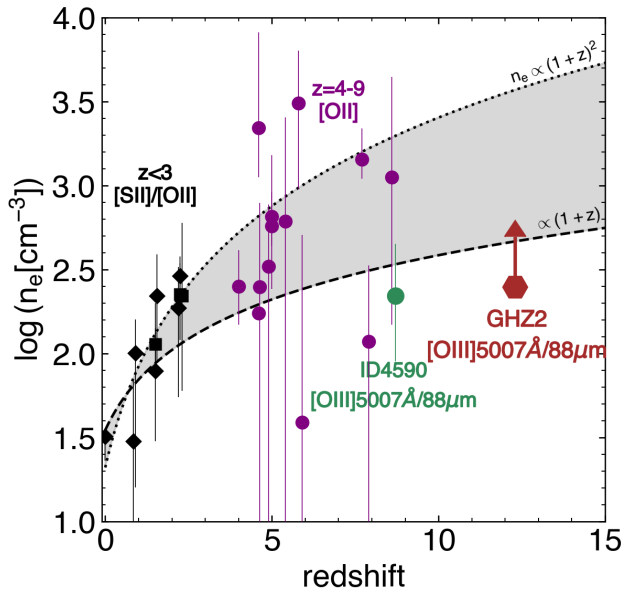


Figure 6: **The redshift evolution of the electron density.** Compilation of spectroscopically-derived measurements of electron density of ionized gas in galaxies at different redshifts (modified from ref.<sup>58</sup>) along with the constraints inferred for our target, GHZ2, at  $z = 12.36$ . Our results support the evolution towards higher electron densities at high redshifts, which might be associated with the high ionization parameters and high star formation rate surface densities of the bright population of high-redshift galaxies recently discovered with JWST.

37. Cole, J. W. *et al.* CEERS: Increasing Scatter along the Star-Forming Main Sequence Indicates Early Galaxies Form in Bursts. *arXiv e-prints* arXiv:2312.10152 (2023).

38. Finkelstein, S. L. *et al.* The Complete CEERS Early Universe Galaxy Sample: A Surprisingly Slow Evolution of the Space Density of Bright Galaxies at  $z \sim 8.5$ -14.5. *arXiv e-prints* arXiv:2311.04279 (2023).

39. Adams, N. J. *et al.* EPOCHS Paper II: The Ultraviolet Luminosity Function from  $7.5 < z < 13.5$  using 180 square arcminutes of deep, blank-fields from the PEARLS Survey and Public JWST data. *arXiv e-prints* arXiv:2304.13721 (2023).

40. Bergamini, P. *et al.* The GLASS-JWST Early Release Science Program. III. Strong-lensing Model of Abell 2744 and Its Infalling Regions. *Astrophys. J.* **952**, 84 (2023).

41. Reddy, N. A. *et al.* The Effects of Stellar Population and Gas Covering Fraction on the Emergent Ly $\alpha$  Emission of High-redshift Galaxies. *Astrophys. J.* **926**, 31 (2022).

42. Kennicutt, R. C. & Evans, N. J. Star Formation in the Milky Way and Nearby Galaxies. *Annual Review of Astronomy and Astrophysics* **50**, 531–608 (2012).

43. Nagao, T., Maiolino, R. & Marconi, A. Gas metallicity diagnostics in star-forming galaxies. *Astron. Astrophys.* **459**, 85–101 (2006).

44. Maiolino, R. *et al.* AMAZE. I. The evolution of the mass-metallicity relation at  $z \lesssim 3$ . *Astron. Astrophys.* **488**, 463–479 (2008).

45. Sanders, R. L., Shapley, A. E., Topping, M. W., Reddy, N. A. & Brammer, G. B. Direct  $T_e$ -based Metallicities of  $z = 2$ –9 Galaxies with JWST/NIRSpec: Empirical Metallicity Calibrations Applicable from Reionization to Cosmic Noon. *Astrophys. J.* **962**, 24 (2024).

46. Hirschmann, M., Charlot, S. & Somerville, R. S. High-redshift metallicity calibrations for JWST spectra: insights from line emission in cosmological simulations. *Mon. Not. R. Astron. Soc.* **526**, 3504–3518 (2023).

47. Nakajima, K. *et al.* EMPRESS. V. Metallicity Diagnostics of Galaxies over  $12 + \log(\text{O}/\text{H}) = 6.9$ -8.9 Established by a Local Galaxy Census: Preparing for JWST Spectroscopy. *Astrophys. J. Suppl.* **262**, 3 (2022).

48. Schaerer, D., Fragos, T. & Izotov, Y. I. X-ray binaries as the origin of nebular He II emission in low-metallicity star-forming galaxies. *Astron. Astrophys.* **622**, L10 (2019).

49. Simmonds, C., Schaerer, D. & Verhamme, A. Can nebular He II emission be explained by ultra-luminous X-ray sources? *Astron. Astrophys.* **656**, A127 (2021).

50. Lecroq, M. *et al.* Nebular emission from young stellar populations including binary stars. *Mon. Not. R. Astron. Soc.* **527**, 9480–9504 (2024).

51. Upadhyaya, A. *et al.* Evidence for Very Massive Stars in extremely UV-bright star-forming galaxies at  $z \sim 2.2$  – 3.6. *arXiv e-prints* arXiv:2401.16165 (2024).

52. Hirschmann, M. *et al.* Synthetic nebular emission from massive galaxies - II. Ultraviolet-line diagnostics of dominant ionizing sources. *Mon. Not. R. Astron. Soc.* **487**, 333–353 (2019).

53. Übler, H. *et al.* GA-NIFS: A massive black hole in a low-metallicity AGN at  $z \sim 5.55$  revealed by JWST/NIRSpec IFS. *Astron. Astrophys.* **677**, A145 (2023).

54. Ono, Y. *et al.* Morphologies of Galaxies at  $z \gtrsim 9$  Uncovered by JWST/NIRCam Imaging: Cosmic Size Evolution and an Identification of an Extremely Compact Bright Galaxy at  $z \sim 12$ . *Astrophys. J.* **951**, 72 (2023).

55. Bakx, T. J. L. C. *et al.* Deep ALMA redshift search of a  $z \sim 12$  GLASS-JWST galaxy candidate. *Mon. Not. R. Astron. Soc.* **519**, 5076–5085 (2023).

56. Popping, G. An upper limit on [O III] 88  $\mu\text{m}$  and 1.2 mm continuum emission from a JWST  $z \approx 12$ -13 galaxy candidate with ALMA. *Astron. Astrophys.* **669**, L8 (2023).

57. Kaasinen, M., Bian, F., Groves, B., Kewley, L. J. & Gupta, A. The COSMOS-[O II] survey: evolution of electron density with star formation rate. *Mon. Not. R. Astron. Soc.* **465**, 3220–3234 (2017).

58. Isobe, Y. *et al.* Redshift Evolution of Electron Density in the Interstellar Medium at  $z \sim 0$ -9 Uncovered with JWST/NIRSpec Spectra and Line-spread Function Determinations. *Astrophys. J.* **956**, 139 (2023).

59. Reddy, N. A., Topping, M. W., Sanders, R. L., Shapley, A. E. & Brammer, G. A JWST/NIRSpec Exploration of the Connection between Ionization Parameter, Electron Density, and Star-formation-rate Surface Density in  $z = 2.7\text{--}6.3$  Galaxies. *Astrophys. J.* **952**, 167 (2023).
60. Asplund, M., Grevesse, N., Sauval, A. J. & Scott, P. The Chemical Composition of the Sun. *Annual Review of Astronomy and Astrophysics* **47**, 481–522 (2009).
61. Kendrew, S. *et al.* The Mid-Infrared Instrument for the James Webb Space Telescope, IV: The Low-Resolution Spectrometer. *PASP* **127**, 623 (2015).
62. Beiler, S. A. *et al.* The First JWST Spectral Energy Distribution of a Y Dwarf. *Astrophys. J. Lett.* **951**, L48 (2023).
63. Pillepich, A. *et al.* Simulating galaxy formation with the IllustrisTNG model. *Mon. Not. R. Astron. Soc.* **473**, 4077–4106 (2018).
64. Matthee, J. *et al.* The production and escape of Lyman-Continuum radiation from star-forming galaxies at  $z \sim 2$  and their redshift evolution. *Mon. Not. R. Astron. Soc.* **465**, 3637–3655 (2017).
65. Matthee, J. *et al.* EIGER. II. First Spectroscopic Characterization of the Young Stars and Ionized Gas Associated with Strong  $H\beta$  and [O III] Line Emission in Galaxies at  $z = 5\text{--}7$  with JWST. *Astrophys. J.* **950**, 67 (2023).
66. Robertson, B. E. *et al.* New Constraints on Cosmic Reionization from the 2012 Hubble Ultra Deep Field Campaign. *Astrophys. J.* **768**, 71 (2013).
67. Pérez-González, P. G. *et al.* Stellar populations in local star-forming galaxies - I. Data and modelling procedure. *Mon. Not. R. Astron. Soc.* **338**, 508–524 (2003).
68. Pérez-González, P. G. *et al.* The Stellar Mass Assembly of Galaxies from  $z = 0$  to  $z = 4$ : Analysis of a Sample Selected in the Rest-Frame Near-Infrared with Spitzer. *Astrophys. J.* **675**, 234–261 (2008).
69. Pérez-González, P. G. *et al.* What is the nature of Little Red Dots and what is not, MIRI SMILES edition. *arXiv e-prints* arXiv:2401.08782 (2024).
70. Bruzual, G. & Charlot, S. Stellar population synthesis at the resolution of 2003. *Mon. Not. R. Astron. Soc.* **344**, 1000–1028 (2003).
71. Chabrier, G. Galactic Stellar and Substellar Initial Mass Function. *PASP* **115**, 763–795 (2003).
72. Calzetti, D. *et al.* The Dust Content and Opacity of Actively Star-forming Galaxies. *Astrophys. J.* **533**, 682–695 (2000).
73. Ferland, G. J. *et al.* CLOUDY 90: Numerical Simulation of Plasmas and Their Spectra. *PASP* **110**, 761–778 (1998).
74. Chatzikos, M. *et al.* The 2023 Release of Cloudy. *Rev. Mexic. Astron. Astrof.* **59**, 327–343 (2023).
75. Carnall, A. C., McLure, R. J., Dunlop, J. S. & Davé, R. Inferring the star formation histories of massive quiescent galaxies with BAGPIPES: evidence for multiple quenching mechanisms. *Mon. Not. R. Astron. Soc.* **480**, 4379–4401 (2018).
76. Boquien, M. *et al.* CIGALE: a python Code Investigating GALaxy Emission. *Astron. Astrophys.* **622**, A103 (2019).
77. Ferland, G. J. *et al.* The 2017 Release Cloudy. *Rev. Mexic. Astron. Astrof.* **53**, 385–438 (2017).
78. Luridiana, V., Morisset, C. & Shaw, R. A. PyNeb: a new tool for analyzing emission lines. I. Code description and validation of results. *Astron. Astrophys.* **573**, A42 (2015).
79. Yoon, I. *et al.* ALMA Observation of a  $z \gtrsim 10$  Galaxy Candidate Discovered with JWST. *Astrophys. J.* **950**, 61 (2023).